ORIGINAL PAPER

Sylvain Larose · Sheikh A. Akbar

Synthesis and electrical properties of dense Bi$_2$Al$_4$O$_9$

Abstract Bi$_2$Al$_4$O$_9$ ceramics are difficult to sinter to greater than 80% theoretical density due to peritectic decomposition at 1,070 °C. A novel processing method is discussed where a high-bismuth oxide-based liquid is used as a sintering aid. After sintering, the high bismuth oxide phase is removed by leaching with 40% acetic acid. The resulting samples are phase pure and ~91% dense. The grain size varies in a wide range with the average grain size of ~1 μm. The electrical properties of these ceramics were measured as functions of temperature (550–850 °C) and oxygen partial pressure (6×10^{-6}– 1 atm). The total conductivity was separated into electronic and ionic contributions. The low ionic conductivity indicates that the material is not an 'intrinsically defective fast ion conductor'. The ionic conductivity is due almost exclusively to compensating oxygen vacancies related to impurities. With increasing temperature and decreasing oxygen partial pressure, the electronic conduction dominates over the ionic conduction.

Keywords Bi$_2$Al$_4$O$_9$ · Mixed conduction · Impedance spectroscopy · High temperature ion conducting ceramic

S. Larose (✉)
Effensys Inc. and Department of Chemical Engineering,
Université du Québec à Trois-Rivières,
Trois-Rivières, QC Canada G9A 5H7,
E-mail: larose.sylvain@sympatico.ca
Tel.: +1-819-3760742
Fax: +1-819-3763828

S. A. Akbar
Department of Materials Science and Engineering,
The Ohio State University,
Columbus, OH 43210, USA
E-mail: akbar.1@osu.edu

Introduction

Mixed ionic-electronic conduction in oxides

The total conductivity, σ_T, of an oxide material for a given temperature, T, can be expressed as:

$$\sigma_T = \sigma_{\text{ion, T}} + C_T(pO_2)^{\pm 1/m} \tag{1}$$

where $\sigma_{\text{ion,T}}$ is the ionic conductivity, $C_T(pO_2)^{\pm 1/m}$ is the electronic conductivity, and C_T is a temperature-dependent constant. The value of m depends on the relative concentrations of the various types of point defects. The sign in front of $1/m$ is negative when the electronic conductivity is primarily due to excess electrons (n-type) and positive when it is primarily due to electron holes (p-type). When the ionic and electronic contributions to the total conductivity are comparable, the material is said to be a mixed conductor.

Bi$_2$Al$_4$O$_9$ vs. Bi$_4$V$_2$O$_{11}$

Very high oxygen ion conductivity has been reported in the layered, Aurivillius phase, Bi$_4$V$_2$O$_{11}$. At 550 °C, the ionic conductivity of the doped Bi$_4$V$_2$O$_{11}$ reaches 0.1 Ω^{-1} cm^{-1} [1–4]. Unfortunately, Bi$_4$V$_2$O$_{11}$ is not thermodynamically stable at very low oxygen partial pressures, and therefore is not suitable in contact with hydrogen as needed in fuel cells. Another layered compound Bi$_2$Al$_4$O$_9$ has a structure similar to that of Bi$_4$V$_2$O$_{11}$. Instead of alternating layers of Bi$_2$O$_2^{2+}$ sheets and VO$_{3.5}^{2-}$ perovskite blocks, Bi$_2$Al$_4$O$_9$ consists of Bi$_2$Al$_2$O$_{5.5}^+$ and spinel-like AlO$_2^-$ layers. This layering may be conducive to oxide-ion conductivity, especially along the Bi$_2$Al$_2$O$_{5.5}^+$ layers. Since the Bi$_2$Al$_4$O$_9$ phase contains a large number of Al–O bonds, it is expected to be more stable than the vanadate compound at low oxygen partial pressures.

Challenge in making dense, phase pure $Bi_2Al_4O_9$

In the published Bi_2O_3–Al_2O_3 phase diagram, the $Bi_2Al_4O_9$ phase is reported to decompose at about 1,070 °C [5]. The sintering kinetics of $Bi_2Al_4O_9$ are very slow at this maximum temperature, which makes the fabrication of dense bodies of this material a challenge. The only reported synthesis of $Bi_2Al_4O_9$ ceramics starts with bismuth oxide-rich powders produced by the glycine nitrate combustion method [6]. Despite attempts for the synthesis of single-phase ceramics, some high bismuth oxide phases remain in the sintered samples of $Bi_2Al_4O_9$. We refined the synthesis and fabrication of these ceramics by developing a method for the removal of the excess bismuth oxide.

Materials and methods

Powder synthesis, sintering and leaching of minor phase

Bismuth aluminate powders were produced from mixtures of nitrates by the glycine nitrate process (GNP) [7, 8] in a 4-L stainless steel beaker. Powders of nominal composition $Bi_{2.224}Al_4O_{9.336}$ were prepared using 11.36 g bismuth nitrate, 16.00 g aluminum nitrate, 20.38 g glycine, 10 mL nitric acid (70.9 vol% in aqueous solution), and 100 mL Millipore distilled water. The excess bismuth with respect to the stoichiometric composition $Bi_2Al_4O_9$ is used to produce a Bi-rich liquid acting as a sintering aid. The composition $Bi_{2.224}Al_4O_{9.336}$ (11.2% molar excess Bi_2O_3 with respect to $Bi_2Al_4O_9$) led to the highest-density pellet after the leaching step (see below). After combustion, the voluminous, multi-colored char was ground using mortar and pestle. The powder was calcined in an open Pt crucible at 750 °C for 10 h. The typical yield was about 7.5 g.

The powders were characterized by X-ray diffraction (XRD) and scanning electron microscopy (SEM) in terms of composition, grain morphology, and grain size. Energy dispersive spectrometry (EDS) analyses were performed on selected grains. X-ray maps were also produced to verify sample homogeneity.

The effect of compaction pressure and calcining time on pellet density were evaluated. The optimum compaction pressure was about 97 MPa (14 kpsi). The powder sintering time which led to the highest pellet density (95%, measured by Archimedes' method) was 12 h at 1,050 °C. Polished and fractured sections of the pellets were characterized in terms of phase distribution by SEM and XRD.

The effect of acetic acid solution on the stability of $Bi_{24}Al_2O_{39}$ and $Bi_2Al_4O_9$ was studied. First, the stability of stoichiometric $Bi_2Al_4O_9$ during the leaching process was tested. About 1.25 g of powder was stirred in 500 mL of acetic acid (20 vol.% in aqueous solution) for 10–12 h. Magnetic stirring was used to enhance mixing. The powder was characterized by XRD after the experiment. The metal cation content of the leachate was analyzed by complexometric titration using pyrocatechol violet as the indicator. Secondly, the acetic acid (100, 70, 40 and 20 vol.% in water) was used to remove the Bi-rich phase from powders and 2-mm-thick sintered "composite" pellets that had an initial nominal composition of $Bi_{2.224}Al_4O_{9.336}$. Typically, the quantity of leaching solution was 600 mL/g of pellet. Two samples were immersed in each solution for 1 week. The leached pellets were characterized in terms of density, phase distribution, and homogeneity by SEM and XRD.

Impedance measurements

Platinum electrodes (~1 μm thick) were sputtered onto polished surfaces of stoichiometric $Bi_2Al_4O_9$ disks and annealed at 850 °C for 1 week in air. Impedance measurements were taken with a Solartron 1260 Frequency Response Analyzer (FRA) in the frequency range of 100 mHz–5 MHz as a function of oxygen partial pressures (6×10^{-6}–1 atm, from premixed Ar/O_2 gases; same atmosphere on both sides of the cell) and temperature (550–850 °C).

The span of a semicircle on the real axis of a Nyquist (impedance, Z^*) plot corresponds to the resistance (R) of its associated conduction process. Plotting the resistance (or the corresponding conductivity) on an Arrhenius plot leads to the determination of the activation energy (E_a) for the electrochemical process. The Nyquist plot is not the only representation of the response of a cell to an AC perturbation. Other functions can be derived from the impedance data, and can be plotted in other complex planes. These functions are:

$$Admittance : Y^* = 1/Z^* \qquad (2)$$

$$Capacitance : C^* = 1/(i\omega Z^*) \qquad (3)$$

$$Modulus : M^* = i\omega Z^* \qquad (4)$$

Where, $i = \sqrt{-1}$ is the complex quantity. Multiplane analysis resolves relaxation behaviors that are difficult to discern in the impedance plane alone. The data can also be plotted in the Bode plane (log |Z| vs. log(ω)) to clearly show the frequency distribution.

The data obtained in this work were plotted in the impedance, admittance, capacitance, and modulus planes. The lattice resistances derived from the Nyquist plots (in the impedance plane) were used to produce plots displaying the temperature- and pO_2-dependences of the conductivity. The temperature and pO_2-dependences of the depression angle were also plotted.

The critical frequency, f_c, for an electrochemical process is defined as the frequency at the maximum of the impedance arc associated with the relaxation process. Plotting f_c as a function of $1/T$ is another way to determine E_a since the slope of this plot is proportional to E_a. The relaxation time, τ, of an electrochemical

process can be calculated from the value of the critical frequency:

$$\tau = 1/(2\pi f_c) \tag{5}$$

Lattice (intragranular) and grain-boundary (intergranular) resistance and capacitance were calculated from the Z^* plot. Other important electrical parameters were calculated using a complex, nonlinear, least-square (CNLS) curve-fitting software program, which was developed at The Ohio State University. Unlike most commercial software, this program calculates all the electrical parameters without using an equivalent circuit [9]. This characteristic allows a more general analysis of an electrochemical system.

Non-equilibrium resistance measurements

Non-equilibrium resistance measurements were taken in order to separate the formation and migration components of the activation energy for the electronic conduction. Such an experiment also leads to the calculation of a value for the enthalpy change associated with the formation of oxygen vacancies and excess electrons. At very high heating and cooling rates, and for short times, the concentration of electronic defects does not change significantly. As a result, the electronic migration energy ($E_{mig}(e^-)$) can be estimated from the slope in the Arrhenius plot obtained from these non-equilibrium tests. The value for $E_{mig}(e^-)$ is obtained once the ionic contribution to the total conductivity is subtracted. Because the heating and cooling rates must be high, the use of the FRA is not suited for this experiment. A multimeter was used instead. Measurements were taken at temperatures and pO_2s for which the DC resistance across the cell did not differ significantly from the lattice resistance, thus under conditions for which electrode interface and grain boundary resistances are negligible with respect to the lattice resistance. The sample was subjected to various heating and cooling rates. Arrhenius slopes that are independent of the rate mean a negligible change in the excess electron concentration as the temperature changes. Therefore, a rate-independent slope is a measure of the migration energy.

Results and discussions

Characterization of the material

A micrograph of the powder before compaction is shown in Fig. 1. The average grain size was about 0.2 μm. The grain size distribution was rather wide (~0.05 to 0.5 μm) and appeared to be bimodal. The difference between the observed disk density (~95%) and the theoretical density may be related to many factors. Among them are slow diffusion kinetics and the effect of the wide grain distribution. The former is due to the relatively low temperature at which $Bi_2Al_4O_9$ had to

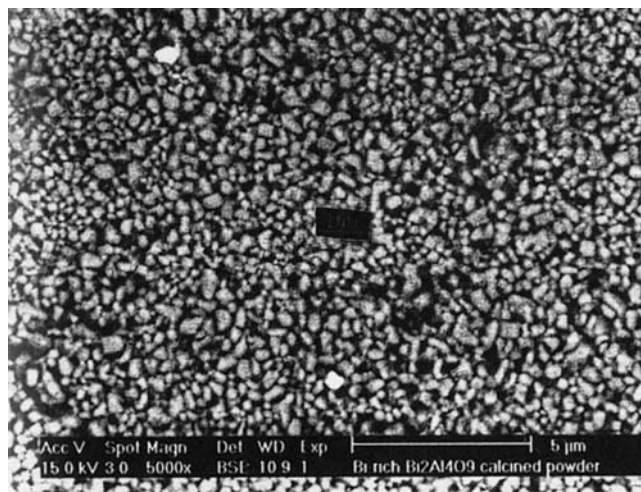**Fig. 1** SEM backscattered electron image (BEI) micrograph of calcined $Bi_2Al_4O_9$. Magnification: ×5,000. The average grain size is ~0.2 μm

be sintered to avoid decomposition. The latter is due to the powder preparation method and is hard to control.

A micrograph showing the backscattered electron image (BEI) of a fractured sintered disk is illustrated in Fig. 2. This micrograph and EDS analyses indicate that the material consists of large (~10 μm) and small (~1 μm) $Bi_2Al_4O_9$ grains. The micrograph also shows a light-colored phase between some $Bi_2Al_4O_9$ grains. Based on the BEI and EDS data, the intergranular phase is found to contain a high concentration of Bi. The precise stoichiometry of the intergranular phase was not determined due to its limited amount. The presence of $Bi_{24}Al_2O_{39}$ or some other Bi-rich material in the intergranular space is consistent with the microscopic observations. The micrograph of a polished section (Fig. 3) shows that the residual pores (darkest areas) in
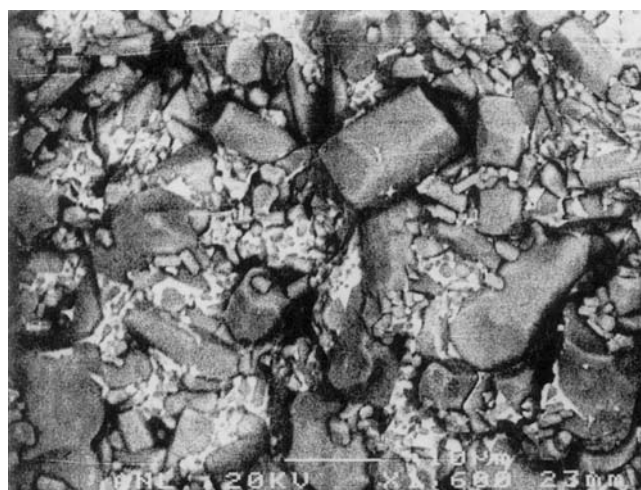

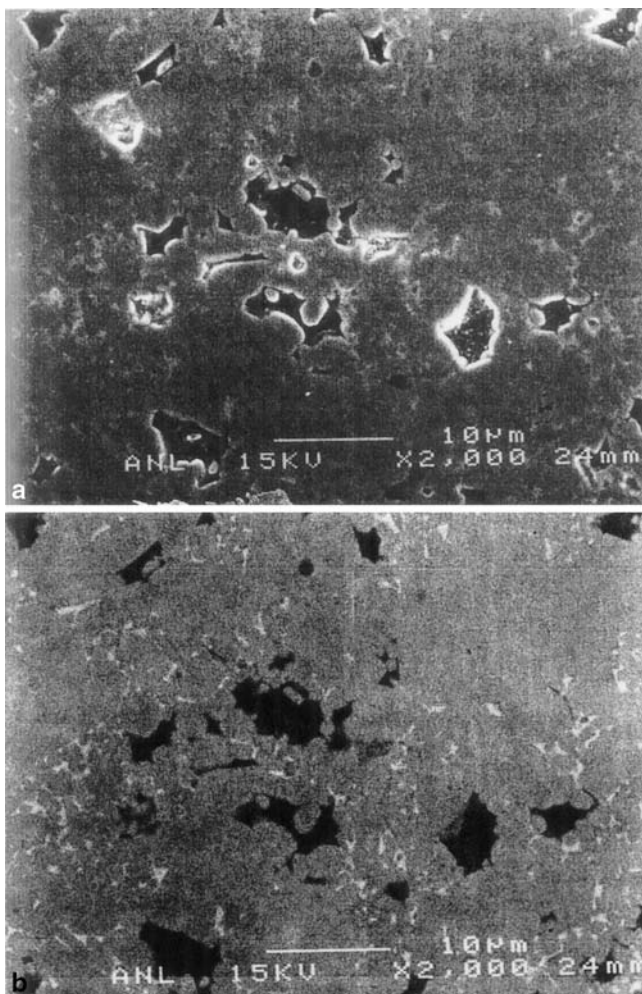**Fig. 2** BEI micrograph of a fractured section of a sintered Bi-rich $Bi_2Al_4O_9$ sample prepared by the GNP method. Magnification: ×1,600

Fig. 3 Secondary electron image (SEI) micrograph of a polished section of a sintered Bi-rich $Bi_2Al_4O_9$ sample prepared by the GNP method. Magnification: ×2,000

the sintered disk are large (2–5 μm) and isolated. The micrograph also shows the light-colored $Bi_{24}Al_2O_{39}$ or some other Bi-rich phase between some $Bi_2Al_4O_9$ grains (gray colored).

Leaching experiment

After the leaching attempt on the stoichiometric $Bi_2Al_4O_9$ powder, no bismuth was detected by titration of the "would-be" leachate. Part of the remaining solution was concentrated by a factor of 10. Again, no bismuth was detected. This result shows that the Bi concentration was below the detection limit. An estimate of this limit indicates that less than 0.1% of the initial quantity of Bi^{3+} cations were removed by the leaching process. Thus, the effect of the leaching process on the $Bi_2Al_4O_9$ phase is negligible.

The yellow color of the Bi-rich phase either on the surface of the pellets or in the cross-sections served as the primary indicator of extent of leaching for the experiments carried out with pellets. Surface-only leaching was observed for the 100% acetic acid experiment. Insignificant color removal was found after 1 week in 20% acetic acid. Complete color removal was obtained after exposure to 40% and to 70% acetic acid. The failure to obtain significant leaching using 100% acetic acid indicates that a certain amount of water is necessary for effective color (i.e., bismuth-rich phase) removal. The results also indicate that the minimum amount of acid needed for the effective leaching is between 20% and 40%. After 1 week in the 40% or in the 70% solutions, the pellet density decreased by about 3–4%, leading to 88–91% dense disks. The XRD of a leached pellet showed $Bi_2Al_4O_9$ only; no other phases were detected. The titration analysis of the leachate indicated that the quantity of cations (total, i.e., Bi + Al) dissolved by the acid is consistent with the weight loss measured (within 1% error) if it was due to the leaching of the $Bi_{24}Al_2O_{39}$ phase.

A BEI micrograph of a polished cross-section of a leached disk is shown in Fig. 4. Comparing Figs. 3 and 4, all the excess bismuth oxide was removed by the leaching process. Micrographs of a fractured surface of a leached disk are shown in Fig. 5. An Al-rich, amorphous-looking phase was formed at a few locations during the leaching step. This phase is seen near the surface of the sample in Fig. 5b. The BEI micrographs show that only a few (less than 1% of the volume) isolated pockets of a phase rich in Al were observed in the bulk of the sample; the rest of the bulk had the $Bi_2Al_4O_9$ stoichiometry. The Al-rich phase does not appear to be continuous at all, unless a very thin (few nanometers) layer is present everywhere, but this possibility seems very unlikely because: (1) we observe a continuous network of well-joined ("welded") $Bi_2Al_4O_9$ grains on the micrographs of polished samples; and (2) the IS spectra

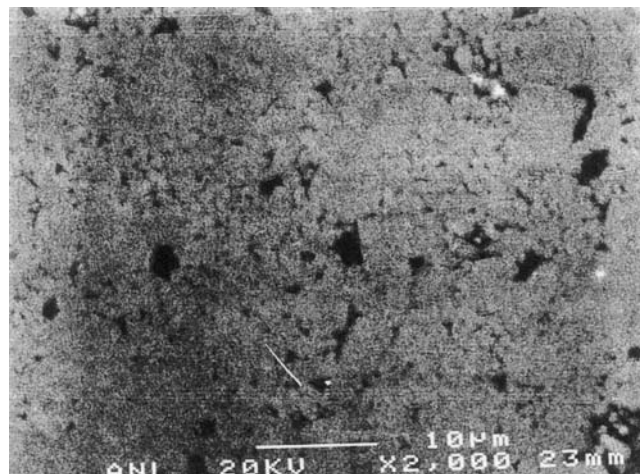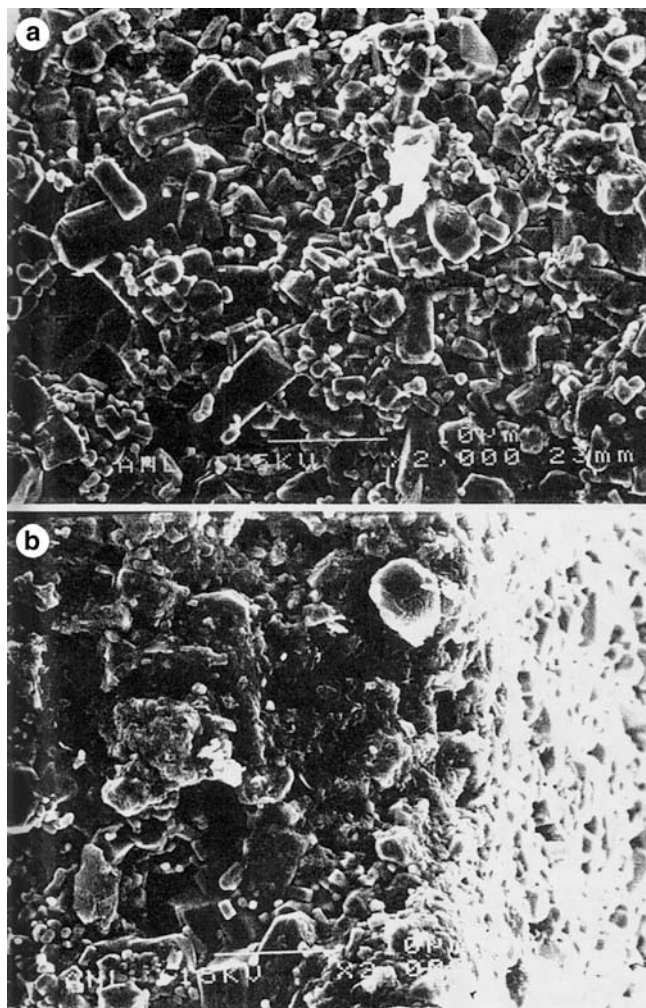**Fig. 4** SEI micrograph of a polished section of a leached $Bi_2Al_4O_9$ sample prepared by the GNP method

Fig. 5 SEI micrographs of fractured sections of a leached $Bi_2Al_4O_9$ sample. **a** Bulk of the sample, **b** edge of the sample. Magnification: ×2,000

of the disks (see below) do not show any extra arc that would be associated with a significantly resistive intergranular phase.

Electrical properties

Measured electrical data plotted in the Z^*, Bode, and Y^* planes are shown in Fig. 6. Semicircular relaxations were observed only in the Z^* plane. At all temperatures and oxygen partial pressures, the Z^* plots show two semicircles, with the left semicircle (high frequency) larger than the right one (low frequency).

The electrical measurements were repeated with a disk that had a different geometry to determine what type of resistance, bulk or electrode interface, is associated with each arc. If the electrodes are applied reproducibly, and all the other experimental parameters kept constant, the ratio, α, of real-axis intercepts for a bulk process is proportional to the ratio of the thickness to the area for each arc. That is

$$\alpha = R_1/R_2 = d_1A_2/d_2A_1 \tag{6}$$

where R_i, d_i, and A_i ($i = 1$ or 2) are the resistance, thickness, and area of each disk, respectively. Given the geometries of the two disks employed, the theoretical α-values for the bulk and electrode processes are 1.27 and 1.75, respectively. The experimental α-values for the high- and low-frequency arcs are ~1.1 and 1.28, respectively. The agreement between the low-frequency-arc experimental α-value and the theoretical bulk α-value shows that the low-frequency arc is due to a bulk process. Although the experimental α-value for the high-frequency arc is not as close to the theoretical bulk α-value (13% difference), it is even farther from the theoretical α-value for the electrode interface process (37% difference). Moreover, the high-frequency arc cannot be associated with an electrode process since electrode processes are always observed at lower frequencies (which means longer relaxation times) than bulk processes. Thus, both arcs are associated with bulk processes, within experimental uncertainties.

Grain boundary polarization is always observed at lower frequencies (longer relaxation times) than lattice polarization. Therefore, the right-side (low frequency) arc was attributed to the grain boundary impedance. The relaxation time for this arc was 0.1 s at 750 °C, which is reasonable for grain boundary processes. The left-side (high frequency) arc is slightly distorted (variable curvature) at low temperature and high pO_2, i.e., when the material is least conductive. Such an effect was extensively studied by Kleitz et al. [10] and Dessemond [11]. The slightly distorted arc is attributed to an overlap between the lattice impedance and the impedance of an intermediate relaxation process, such as that due to pores, voids, or a minor phase. This intermediate relaxation process is significant only at lower conductivity, and is negligible at higher conductivity. The somewhat porous microstructure of the $Bi_2Al_4O_9$ pellets used in this work is responsible for this effect. The modeling calculations included this interference and provided values of lattice conductivity. The magnitude of the resistance associated with the intermediate relaxation process was always less than 20% of the resistance associated with the lattice process. In the Y^* plane, a high-frequency line was associated with the lattice process. The values of the lattice conductivity obtained in the Z^* and Y^* planes agreed very well, as can be seen in Fig. 6 and in Table 1. The relaxation time for the lattice conduction is 10 μs at 750 °C, which is typical of a lattice process. The impedance associated with the intermediate relaxation was negligible with respect to the lattice impedance when the lattice conductivity was higher than ~$3 \times 10^{-6} \Omega^{-1} cm^{-1}$. This conclusion is drawn from the fact that the radius of curvature of the left arc did not change with frequency when the lattice conductivity was this high or higher.

Oxygen partial pressure has a significant effect on the breadth of the arcs on the Nyquist plots, as shown in Fig. 7. The resistances associated with both arcs de-
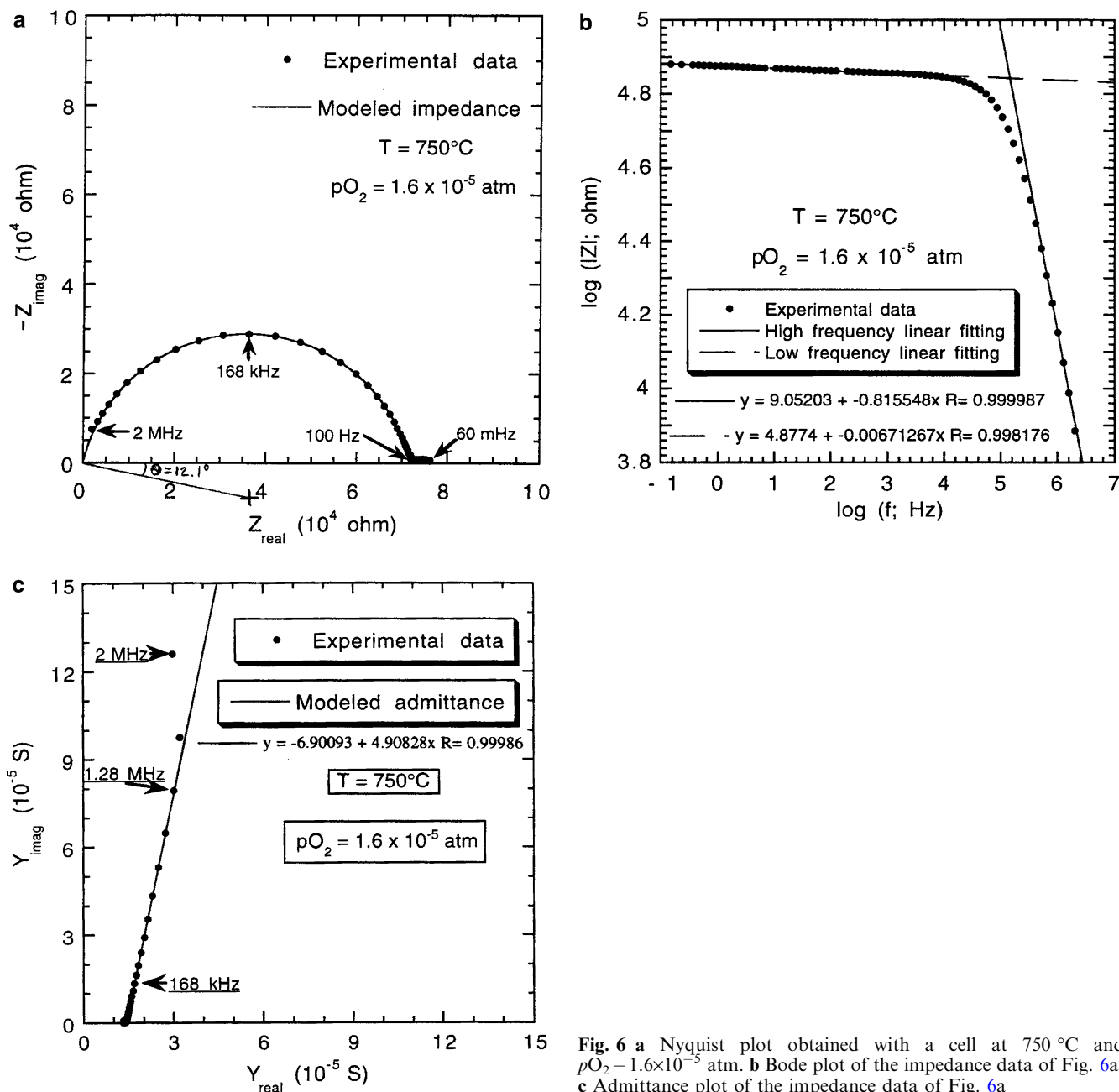
a Experimental data — Modeled impedance, T = 750°C, $pO_2 = 1.6 \times 10^{-5}$ atm. Nyquist plot with markers at 2 MHz, 168 kHz, 100 Hz, 60 mHz, $\Theta = 12.1°$. Axes: $-Z_{imag}$ (10^4 ohm) vs Z_{real} (10^4 ohm).

b T = 750°C, $pO_2 = 1.6 \times 10^{-5}$ atm. Experimental data, High frequency linear fitting, Low frequency linear fitting. $y = 9.05203 + -0.815548x$ R= 0.999987; $y = 4.8774 + -0.00671267x$ R= 0.998176. Axes: log (|Z|; ohm) vs log (f; Hz).

c Experimental data — Modeled admittance. $y = -6.90093 + 4.90828x$ R= 0.99986. T = 750°C, $pO_2 = 1.6 \times 10^{-5}$ atm. Markers at 2 MHz, 1.28 MHz, 168 kHz. Axes: Y_{imag} (10^{-5} S) vs Y_{real} (10^{-5} S).

Fig. 6 a Nyquist plot obtained with a cell at 750 °C and $pO_2 = 1.6 \times 10^{-5}$ atm. **b** Bode plot of the impedance data of Fig. 6a. **c** Admittance plot of the impedance data of Fig. 6a

crease with decreasing oxygen partial pressure. This dependence of resistance on oxygen partial pressure is typical of an n-type conductivity.

The lattice conductivity values are plotted as a function of $1,000/T$ and log pO_2 (see Fig. 8). At 1 atm O_2, the curve in Fig. 8a is nearly linear in the temperature range of 600–750 °C. The activation energy for conduction calculated by linear regression in this temperature range is 1.14 eV. This energy value is for the total conductivity, comprising of both the ionic and the electronic contributions. At higher temperatures, an abrupt change in slope is observed. The activation energy increases to

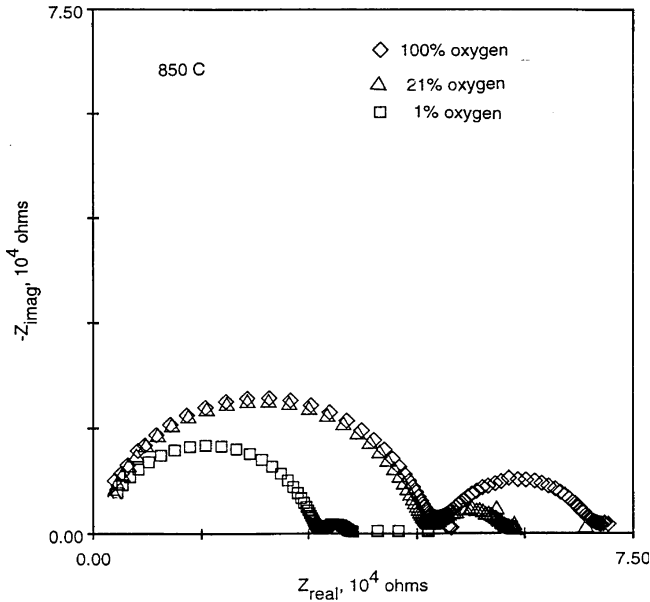| Table 1 Comparison between the resistances obtained from different diagrams at 1.6×10^{-5} atm of oxygen for two temperatures	Nyquist (Ω)	Admittance (Ω)	Bode (Ω)
Lattice at 750 °C	7.16×10^4	7.11×10^4	6.96×10^4
Lattice + intermediate relaxation at 750 °C	7.28×10^4	7.11×10^4	6.96×10^4
lattice at 650 °C	6.40×10^5	6.44×10^5	
Lattice + intermediate relaxation at 650 °C	8.95×10^5	8.94×10^5	

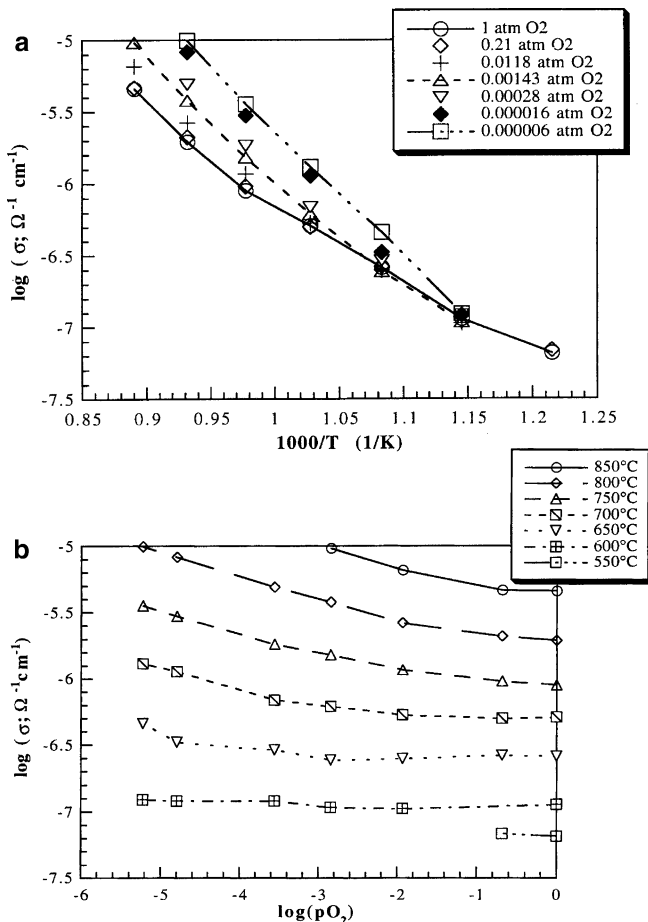**Fig. 7** Typical variation fo the shape and size of the Nyquist plot with respect to pO$_2$

Fig. 8 a Arrhenius plot of the lattice (intragrain) conductivity. **b** Oxygen partial pressure dependance of the lattice (intragrain) conductivity (pO$_2$ in atm)

2.1 eV. This increase in the activation energy points to a change in major conduction mechanism, that is, from oxide ion to electronic conductivity. The change in slope, that is in conduction mechanism, occurs at lower temperatures for lower oxygen partial pressures. Plots showing the pO$_2$- and temperature-dependencies of the critical frequency (Fig. 9) have the same dependencies, and give the same activation energy as those obtained from Fig. 8, within 5% error.

The isothermal plot of conductivity as a function of $(p$O$_2)^{-1/4}$ (see Fig. 10) shows a linear relationship. At 750 °C, the steep slope indicates a high excess electron concentration, leading to the n-type conductivity. The lattice ionic conductivity is dominant at large pO$_2$, i.e., at $(p$O$_2)^{-1/4} \cong 0$. An expression for the lattice ionic conductivity was therefore derived from the least-square calculations performed on the curves given in Fig. 10, expressed in Eq. 7. In Fig. 10, the intercept of each line with the conductivity axis, for $(p$O$_2)^{-1/4} \cong 0$, gives the ionic conductivity at the given temperature.

$$\sigma_{ion} = [154/T]\exp(-1.08\,eV/kT)(\Omega^{-1}cm^{-1}). \tag{7}$$

The small magnitude of the pre-exponential factor reflects the low ionic conductivity, indicating that the material is not an 'intrinsically defective fast ion conductor'.

Since $\sigma_{total} = \sigma_{ion} + \sigma_e$, we obtained an expression for the lattice electronic conductivity, σ_e, by subtracting the ionic conductivity from the total conductivity. This expression is given in Eq. 8.

$$\sigma_e = [5.65 \\ \times 10^6/T]\exp(-2.15\,eV/kT)(pO_2)^{-1/4}(\Omega^{-1}cm^{-1}) \tag{8}$$

The pO$_2$-dependence of σ_e can be used to infer conclusions concerning the relative concentration of point defects. Considering the defect equation giving rise to the n-type electronic conductivity:

$$O_o^x \rightarrow 1/2O_2(g) + V_o^{\cdot\cdot} + 2e^- \tag{9}$$

and its equilibrium constant:

$$K = (pO_2)^{1/2}[V_o^{\cdot\cdot}][e^-]^2 \tag{10}$$

in which the brackets indicate concentrations and the general electroneutrality condition:

$$[V_o^{\cdot\cdot}] = (1/2)[M'_{Al,Bi}] + (1/2)[e^-] \tag{11}$$

where $[M'_{Al,Bi}]$ represents the effective concentration of the relative negative charges due to aliovalent substitutional cations on Al and Bi sites. The effective negative charge is due to predominantly acceptor-type substitutional impurities. Two limiting cases exist for Eq. 11:

Case #1 : If $[V_o^{\cdot\cdot}] \cong (1/2)[e^-]$ \hfill (12)

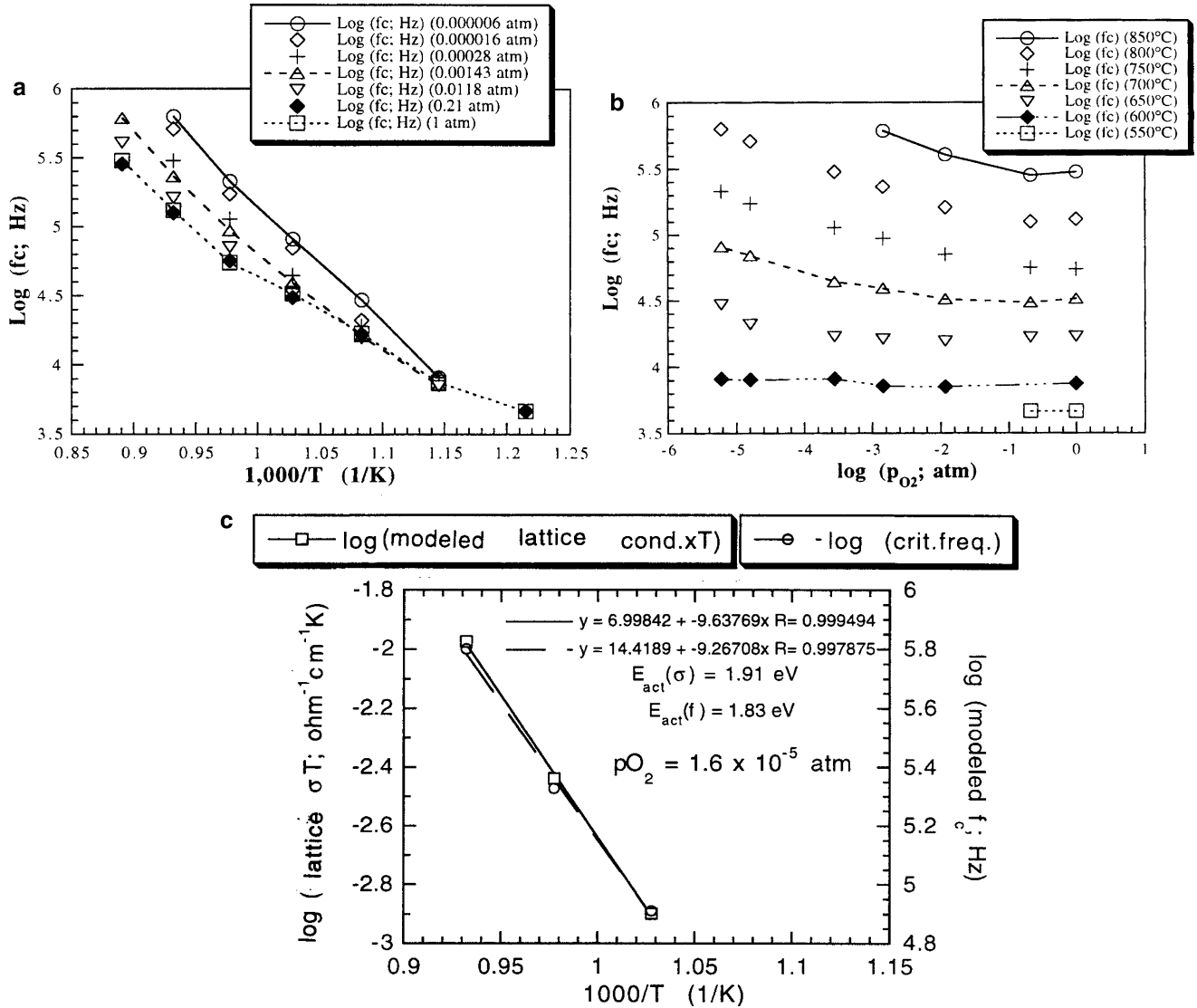then : $K \cong \{(p$O$_2)^{1/2}[e^-]^3\}/2$ \hfill (13)

Fig. 9 a Arrhenius plot of the lattice (intragrain) critical frequency. **b** Oxygen partial pressure dependance of the lattice (intragrain) critical frequency. **c** Comparison between the activation energies obtained with the conductivity and critical frequency plots

and : σ_e varies as $(pO_2)^{-1/6}$. (14)

This case represents an intrinsic behavior.

Case #2 : If $[V_o^{\cdot\cdot}] \cong (1/2)[M'_{Al,Bi}]$ (15)

then : $K \cong K'(pO_2)^{1/2}[e^-]^2$ (16)

where K' is a constant

and : σ_e varies as $(pO_2)^{-1/4}$. (17)

This case represents an extrinsic behavior.

The linear dependence observed in Fig. 10 means that Case#2 applies well in the range of temperatures and pO_2s investigated. Therefore, the ionic conductivity is due almost exclusively to oxygen vacancies acting as compensating defects for acceptor impurities. The main impurities detected by inductively coupled plasma-atomic emission spectrography (ICP-EAS) were Fe (300 ppm), Cu (100 ppm), Sr (80 ppm), Ba (70 ppm), and Ca (40 ppm). Iron is expected to be triply oxidized when occurring as an impurity in $Bi_2Al_4O_9$, and should therefore not affect the concentration of oxygen vacancies. The other impurities, on the other hand, are expected to be present in doubly oxidized (acceptor-type) form, and should be associated with the creation of positively charged oxygen vacancies as charge- and site-compensating defects. Impurity-controlled ionic conductivity has been observed in a number of oxides, such as Nb_2O_5 [12]. In the same manner as $Bi_2Al_4O_9$, Nb_2O_5 exhibits an n-type semiconductivity at high temperature and low pO_2, but is an extrinsic ionic conductor in air. The minimum value of the concentration of oxygen vacancies required to obtain this extrinsic behavior at 900 °C was estimated to be only a few parts per million.

Fig. 10 Plots of the isothermal conductivities as a function of $(pO_2)^{-1/4}$, which corresponds to Case#2
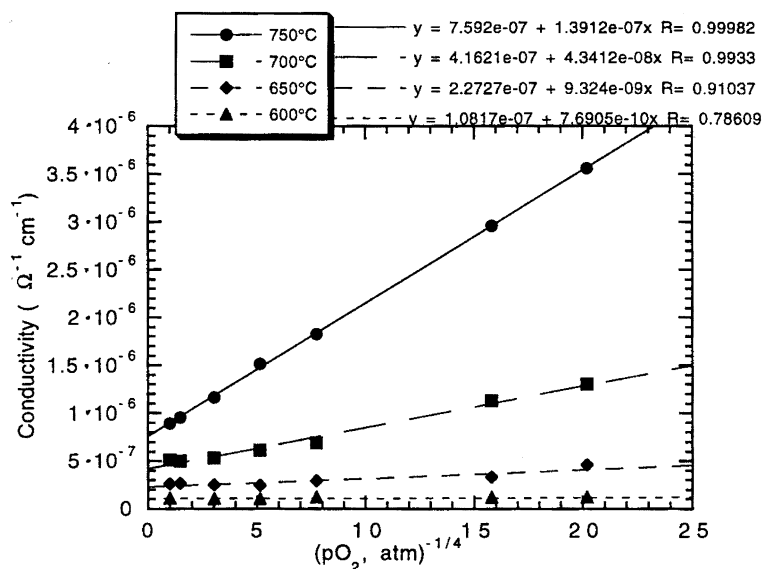
For the sake of comparison, the concentration of oxygen vacancies that compensate the acceptor impurities in $Bi_2Al_4O_9$ was estimated to be in the range from 100 ppm to 200 ppm. This range was determined using the impurity content measured by the ICP-AES and spark source mass spectrometry (SSMS) methods. This defect concentration is large enough to generate an impurity-controlled ionic conductivity in an oxide material.

The electronic transference number was calculated and plotted as a function of temperature and pO_2 (Fig. 11). The calculation clearly indicates that the material becomes more electronically conducting with increasing temperature and decreasing pO_2. All the conductivity data as functions of temperature and oxygen partial pressure were used to produce the domain diagram shown in Fig. 12. At 600 °C, changes in oxygen partial pressure have very little effect on the conductivity. This characteristic is consistent with an electrolytic domain. As temperature increases, the boundary between the n-type domain and the electrolytic domain shifts to higher oxygen partial pressures; electronic conduction is the major charge transport mechanism in the temperature range of 800–850 °C.

The depression angle can also be extracted from the Nyquist plot and used to interpret the electrical behavior. The depression angle of an impedance arc is defined as the angle at which the center of the circular arc is depressed below the real axis. Plotting the temperature-dependence of the depression angle provides useful information about conduction processes. The plotting of pO_2-dependance of the depression angle in Fig. 13 clearly shows that this angle is pO_2-independent at low temperature, whereas it increases with decreasing pO_2 at high temperature. This behavior gives support to a change in the conduction mechanism as the temperature increases, and pO_2 decreases.

Non-equilibrium resistance measurements were conducted to separate the migration (E_{mig}) and formation
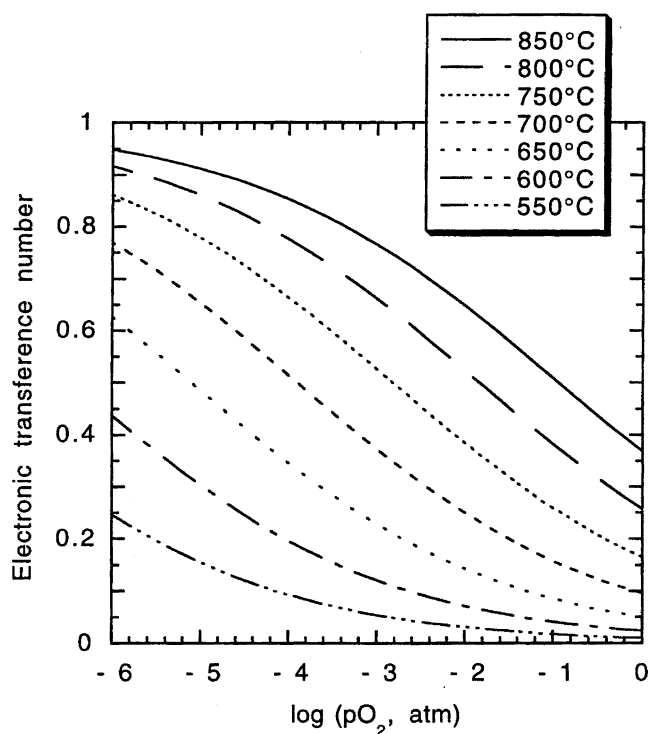

Fig. 11 Oxygen partial pressure-dependence of the ionic transference number

(E_{form}) energy terms of the activation energy for the electronic conduction. The fast heating and cooling rates (3.5–6.3 °C/min) and the short duration (10–15 min) of the heating and cooling steps prevented any significant re-equilibration of the concentration of excess electrons. Indeed, the measured resistances were independent of the heating and cooling rates. In fact, slopes in the Arrhenius plots of non-equilibrium conductivity showed an initial increase upon cooling or heating before becoming
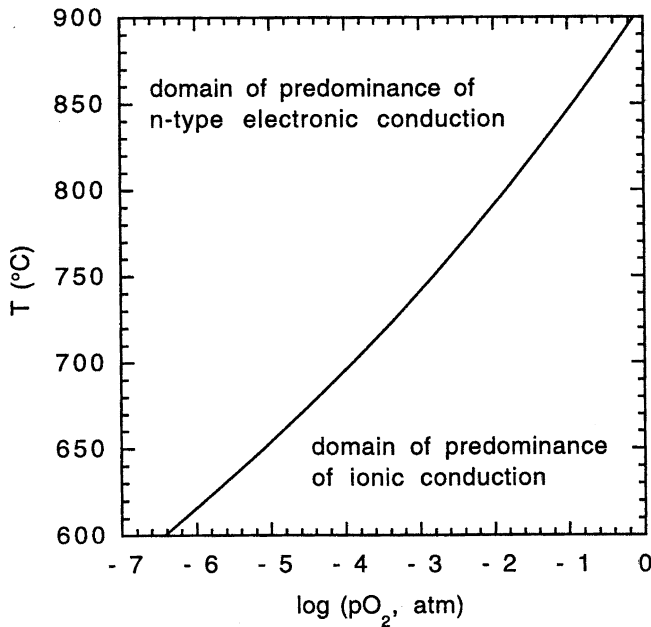
Fig. 12 Domain plot showing the boundary line where the ionic and the electronic conductivities are equal in magnitude

non-equilibrium Arrhenius plots were selected to calculate the electronic migration energy. The temperature was then corrected for the sum of thermal lag and thermal potential. The extrinsic ionic contribution was subtracted from the total conductivity, in order to obtain the electronic contribution. The migration energy was obtained from the slope of the non-equilibrium electronic conductivity plot. The formation energy is obtained by subtracting the migration energy from the total activation energy. The values obtained for the electronic formation and migration energies are given in Eq. 18.

$$E_{form}(e^-) = 0.33\,\text{eV}; E_{mig}(e^-) = 1.82\,\text{eV} \qquad (18)$$

Equation 9 shows the general formation of positively charged oxygen vacancies and excess electrons. The standard enthalpy change associated with this reaction is twice the value of the electronic formation energy. Therefore, the calculated standard enthalpy change of Eq. 9, based on our measurements, is 0.66 eV (64 kJ/mol). This value is consistent with the known low strength of Bi–O bonds and the propensity of Bi-containing oxides to be reduced [13, 14]. This low, experimentally-determined enthalpy value indicates that Bi–O bonds can be easily broken, producing charged oxygen vacancies and associated charge-compensating, excess electrons (e.g., Eq. 9). Thus, the low value is consistent with the high electronic conductivity of the material.

nearly constant. The initial change in slope is due to an increasing thermal lag between the sample and the adjacent thermocouple plus, perhaps, the building of a thermal potential due to a thermal gradient between the sample electrodes. The thermal lag and thermal potential eventually reach constant values when the slope stabilizes. The sum of these two factors was then calculated by extrapolating the linear portion of the curve to the value of equilibrium conductivity at the starting temperature. Sums of thermal lag and thermal potential equivalent to 6–7 °C were recorded. Rate-independent, linear portions of the cooling and heating curves in the

Conclusions

Fine, Bi-rich $Bi_2Al_4O_9$ powder was produced by the glycine nitrate process. The Bi-rich phase enhanced densification of sintered $Bi_2Al_4O_9$ bodies. After sintering, the pellet density was in the range of 92–95% of theoretical value.

Fig. 13 Oxygen partial pressure dependence of the lattice (intragrain) depression angle
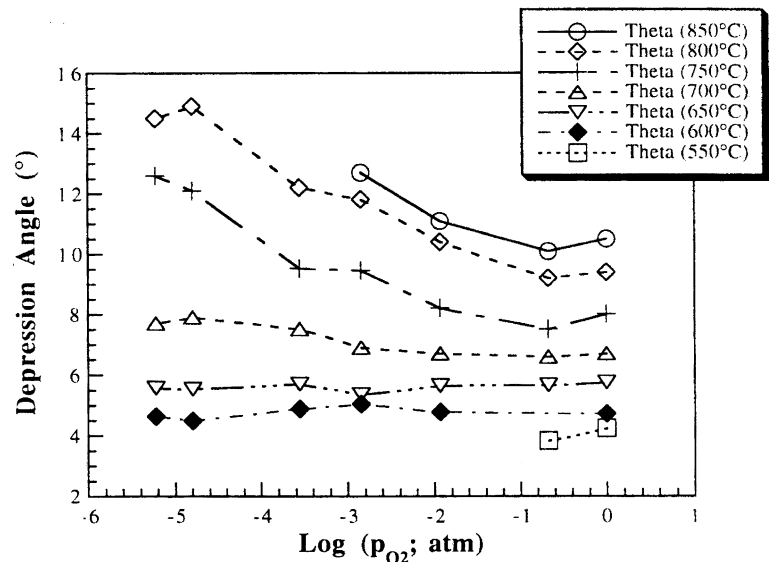
The Bi-rich phase was removed from $Bi_2Al_4O_9$ powders and sintered compacts by leaching with aqueous acetic acid. The $Bi_2Al_4O_9$ phase was shown to be stable in acetic acid solutions. As a result of the leaching process, pellet density decreased 3–4%. Titration and X-ray analyses proved the leaching method to be effective in removing Bi-rich phases, leaving dense, pure $Bi_2Al_4O_9$ pellets. The general approach for removing sintering aids or fluxes may find applications in other Bi-containing materials.

A multiplane analysis performed with Nyquist (resistance and critical frequency), admittance and Bode plots was found self-consistent and provided values for the lattice conductivity of $Bi_2Al_4O_9$. The pO_2- and temperature-dependences of the lattice conductivity allowed modeling according to the classical point defect theory. The conductivity was thus separated into ionic and electronic contributions. The low ionic conductivity of the $Bi_2Al_4O_9$ lattice indicates that the material is not an 'intrinsically defective fast ion conductor'. The ionic conductivity is due almost exclusively to compensating oxygen vacancies controlled by acceptor impurities. With increasing temperature and decreasing pO_2, n-type electronic conduction dominates over ionic conduction. Depression angle behavior and non-equilibrium measurements gave additional support to the point defect-based explanation of the measured $Bi_2Al_4O_9$ lattice conductivity. The low value (0.66 eV) for the enthalpy of formation of oxygen vacancies is consistent with the known low strength of Bi–O bonds and the propensity of the Bi-containing oxides to be reduced, as well as the high electronic conductivity of the material.

References

1. Pernot E, Anne M, Bacmann M, Strobel P, Fouletier J, Vanier RN, Mairesse G, Abraham F, Nowogrocki G (1994) Solid State Ionics 70(71):259
2. Goodenough JB, Manthiram A, Parantharam M, Zhen YS (1992) In: Balkanski M, Takahashi T, Tuller HL (eds) Solid state ionics. Elsevier, Amsterdam, p 17
3. Vanier RN, Mairesse G, Abraham F, Nowogrocki G (1994) Solid State Ionics 70(71):248
4. Ferloni P, Magistris A (1994) J Phys IV 4:C1
5. Speranskaya EI, Skorokov VM, Safronov GM, Gaidukov EN (1970) Inorg Mater (USSR) 6(7):1201
6. Bloom I, Hash MC, Zebrowski JP, Myles KM, Krumpelt M (1992) Solid State Ionics 53–56:1055
7. Chick LA, Pederson LR, Maupin GD, Bates JL, Thomas LE, Exharhos GJ (1990) Mater Lett 10(1–2):6
8. Bates JL, Chick LA, Weber WJ (1992) Solid State Ionics 52:235
9. Zhu W, Wang CC, Akbar SA, Asiaie R, Dutta PK, Alim MA (1996) Jpn J Appl Phys 35:6145
10. Kleitz M, Dessemond L, Steil MC (1995) Solid State Ionics 75:107
11. Dessemond L (1992) Spectroscopie d'impédance des fissures dans la zircone cubique. PhD Thesis, Institut National Polytechnique de Grenoble
12. Kofstad P (1972) Nonstoichiometry, diffusion, and electrical conductivity in binary metal oxides. Wiley, New York
13. Takahashi T, Esaka T, Iwahara H (1977) J Appl Electrochem 7:299
17. Steele BCH (1992) In: Balkanski M, Takahashi T, Tuller HL (eds) Solid state ionics. Elsevier, Amsterdam, p 17